J. Fluid Mech. (1997), *vol.* 350, *pp.* 189–208. Printed in the United Kingdom

Near-wall measurements in a three-dimensional turbulent boundary layer

By DEBORA A. COMPTON[1] AND JOHN K. EATON[2]

[1]Department of Aerospace and Mechanical Engineering,
Boston University, Boston MA 02215, USA

[2]Department of Mechanical Engineering, Stanford University, Stanford CA 94305, USA

(Received 17 March 1996 and in revised form 27 February 1997)

An experiment was performed to measure near-wall velocity and Reynolds stress profiles in a pressure-driven three-dimensional turbulent boundary layer. An initially two-dimensional boundary layer ($Re_\theta \approx 4000$) was exposed to a strong spanwise pressure gradient. At the furthest downstream measurement locations there was also a fairly strong favourable streamwise pressure gradient.

Measurements were made using a specially designed near-wall laser-Doppler anemometer (LDA), in addition to conventional methods. The LDA used short focal length optics, a mirror probe suspended in the flow, and side-scatter collection to achieve a measuring volume 35 μm in diameter and approximately 65 μm long.

The data presented include mean velocity measurements and Reynolds stresses, all extending well below $y^+ = 10$, at several profile locations. Terms of the turbulent kinetic energy transport equation are presented at two profile locations. The mean flow is nearly collateral (i.e. W is proportional to U) at the wall. Turbulent kinetic energy is mildly suppressed in the near-wall region and the shear stress components are strongly affected by three-dimensionality. As a result, the ratio of shear stress to turbulent kinetic energy is suppressed throughout most of the boundary layer. The angles of stress and strain are misaligned, except very near the wall (around $y^+ = 10$) where the angles nearly coincide with the mean flow angle. Three-dimensionality appears to mildly reduce the production of turbulent kinetic energy.

1. Introduction

Three-dimensional turbulent boundary layers have been the subject of considerable research interest recently because of their technological importance and because present models used on flows of engineering interest fail to predict them adequately. A typical pressure-driven three-dimensional turbulent boundary layer is sketched in figure 1. The cross-stream velocity component U_n increases rapidly from zero at the wall to a maximum which occurs close to the wall. In most three-dimensional turbulent boundary layer experiments, the peak U_n is found within 200 viscous lengths of the wall. In some low-Reynolds-number experiments the peak is as low as $y^+ = 30$. We will refer to the region of the three-dimensional turbulent boundary layer below the point of peak crossflow as the near-wall region. The near-wall region is the critical part of the boundary layer: the turbulence production and stress levels reach a maximum there, and the region accounts for the majority of the displacement thickness.

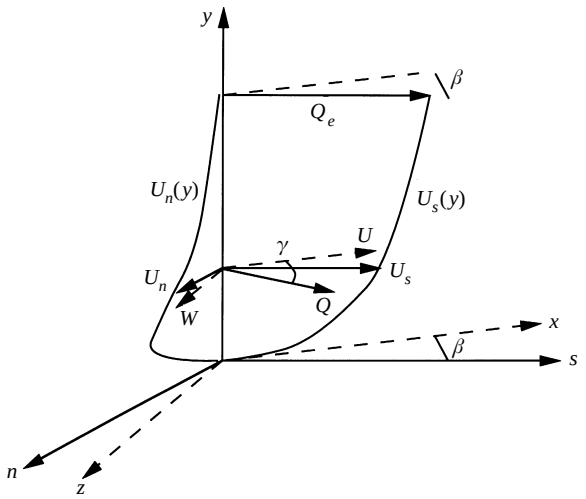

FIGURE 1. The canonical three-dimensional boundary layer.

The most useful models for three-dimensional turbulent boundary layers would be universal streamwise and crossflow mean velocity profiles analogous to the law of the wall. Early attempts to determine a universal crossflow profile have been essentially abandoned, though theoretical limits have been addressed recently by Degani, Smith & Walker (1993). Ölçmen & Simpson (1992) presented a brief review of three-dimensional turbulent boundary layer experiments, and applied several variations of the law of the wall. None of the relations adequately described all of the flows.

Calculation of the mean velocity profiles without the aid of a universal profile requires a turbulence model. One- and two-equation scalar eddy viscosity models are widely used, but are not appropriate for three-dimensional turbulent boundary layers. Virtually every three-dimensional turbulent boundary layer experiment has shown that the shear stress vector (consisting of components $\overline{u'v'}$ and $\overline{v'w'}$) is not aligned with the strain rate vector $\left(\partial U/\partial y, \partial W/\partial y\right)$, as shown in the reviews of Ölçmen & Simpson (1993), Bettelini & Fanneløp (1993), Flack & Johnston (1993), and Compton & Eaton (1995). Simple anisotropic eddy viscosity models have been proposed (cf. Rotta 1977), but generally do not satisfy Galilean invariance. Algebraic stress models and full second-moment closures are needed to capture the anisotropic nature of the turbulence. Boundary layer turbulence structure is distorted by mean flow three-dimensionality, complicating model development (Eaton 1995). For example, the structural parameter $a_1\left(= \left(\overline{u'v'}^2 + \overline{v'w'}^2\right)^{1/2}/q^2\right)$ is consistently lower in three-dimensional turbulent boundary layers than in comparable two-dimensional flows. In some cases where an initially two-dimensional boundary layer is driven to three-dimensionality by a spanwise pressure gradient, the Reynolds stresses fall, despite the imposition of the additional strain rate (cf. Sendstad & Moin 1992).

By the late 1980s, there was some hope that a relatively simple model of the structural distortion might be developed. For example, Anderson & Eaton (1989) proposed that the reduction in a_1 might be controlled by the non-dimensional radius of curvature of a free-stream streamline and that the anisotropy might be controlled by the amount of skewing between the wall and the free stream. At that time there were not enough well-qualified data sets to test such a model. Unfortunately, new experiments have muddled the picture (see the reviews cited above). The imposition

of boundary layer skewing is usually accompanied by additional effects such as longitudinal pressure gradient, wall curvature, or system rotation which impose their own structural distortions on the turbulence. No consistent picture has emerged possibly because the Reynolds stress measurements have been confined to the logarithmic and wake regions of the boundary layer. These regions are especially sensitive to wall curvature and adverse pressure gradients, accounting for the varied behaviour seen in different experiments. Also, the effect of the mean flow three-dimensionality may be fairly weak in the outer flow because the gradient in the crossflow velocity ($\partial W/\partial y$) is small. The three-dimensional effects may be stronger and more consistent in the near-wall region, where $\partial W/\partial y$ is of the same order as $\partial U/\partial y$ and may cause substantial distortion of the turbulence.

It is not known whether the turbulence structure distortions extend into the near-wall region. Johnston (1976) in a review of previous three-dimensional turbulent boundary layer studies found evidence of collateral mean flow near the wall. There is the possibility that the near-wall flow may be unperturbed by boundary-layer skewing. However, the available data are still so sparse that it is impossible to say whether there is a collateral region or whether the turbulence statistics differ from those in two-dimensional boundary layers. To date, there have been only two three-dimensional turbulent boundary layer experiments which include detailed Reynolds stress data below $y^+ = 100$. Flack & Johnston (1993) examined two low-Re_θ three-dimensional turbulent boundary layers in a large water channel using a three-component laser-Doppler velocimeter to obtain data down to $y^+ \approx 8$. They concluded that there is no near-wall collateral region, and that rapid turning of the free-stream velocity has less effect on the turbulent stresses than does slower turning. Their measurements of a_1 collapse onto a single curve below $y^+ = 40$. Ölçmen & Simpson (1994, 1995) developed a high-resolution laser-Doppler anemometer (LDA) to study the near-wall region in the vicinity of a wing–body junction. The complexity of this flow made it difficult to draw general conclusions about the near-wall region.

1.1. *Objectives*

The primary goal of this study was to observe the behaviour of the Reynolds stresses $\overline{u'v'}$ and $\overline{v'w'}$ in the region near the peak cross-stream velocity and approaching the wall, in a moderate-Reynolds-number three-dimensional turbulent boundary layer. With the anticipation that Reynolds stress transport models will eventually provide improved predictions, we also measured triple products (including $\overline{u'^3}$, $\overline{v'^3}$, $\overline{w'^3}$, $\overline{u'^2v'}$, $\overline{u'v'^2}$, $\overline{v'^2w'}$ and $\overline{v'w'^2}$) and streamwise and spanwise derivatives of the Reynolds stresses in order to evaluate terms of the Reynolds stress transport equations. It is the aim of this paper to interpret the data in terms of structure parameters, turning angles, and contributions to the development of turbulent kinetic energy.

2. Facility and experimental methods

The experiment was performed in a closed-circuit wind tunnel operated at 12.5 m s^{-1}, with a 2 ft × 3 ft × 12 ft long test section. The boundary layer studied grows on a horizontal Plexiglas test surface 12 in. above the floor of the tunnel. A 30° Plexiglas wedge placed in the rear of the test section as shown in figure 2 produces the spanwise pressure gradient to turn the streamlines. The wedge spans the entire working height of the test section and blocks exactly half of the test section exit area. A 9.1 in. thick fairing above the test surface relieves some of the favourable pressure gradient

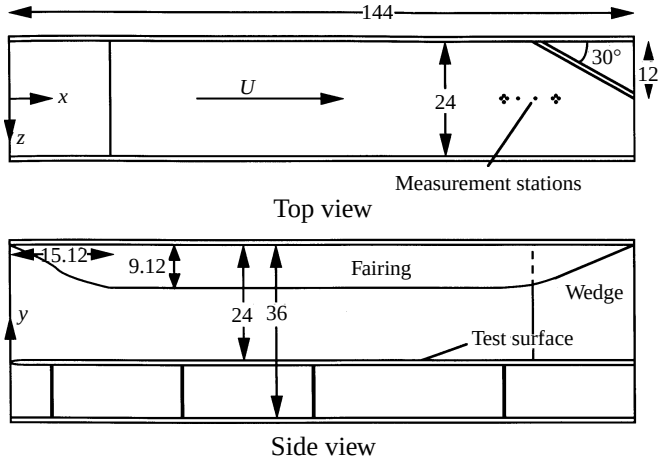

FIGURE 2. Test section (dimensions in inches).

caused by the wedge. The height of the test section increases linearly where the width decreases, so that the open area decreases by a total of 20%.

Two test surfaces were used: one has an array of 89 static pressure taps; the other is clear, for optical access. Both test surfaces used the same 3:2 elliptical nose, with a boundary layer trip placed 6 in. downstream of the leading edge. The boundary layers on the four test section walls were also tripped.

A three-hole pressure probe fabricated from 0.8 mm OD tubes was used to measure mean velocity and skew angle. The probe was calibrated and used in the 'non-nulling' mode, i.e. calibration curves were used to determine the angle and velocity of the approaching flow, without rotating the probe. Two ± 0.5 in. H_2O range pressure transducers (Setra, models 239 and 264), calibrated against a Combist micromanometer, were used for all pressure measurements.

An X-array hot-wire probe, consisting of a DISA 55-P-51 dual-sensor hot-wire tip mounted in a gooseneck probe, was used for the outer-layer turbulence measurements. The two sensor wires are spaced approximately 1.0 mm apart and have an active length of 1.25 mm. TSI IFA-100 constant-temperature bridges were used and the signal was low-pass filtered at 20 kHz. Calibration of the crosswire was performed in the free stream before and after each profile, using the angle calibration procedure described by Westphal & Mehta (1985) and a King's law fit.

During data acquisition, the crosswire probe was aligned with the direction of the mean flow (determined from the three-hole probe) at every point in the profile. The probe tip rotated about its own axis, and we acquired profiles of the boundary layer in four of the probe's 'roll' positions in order to obtain all the components of the Reynolds stress tensor; $\overline{u'v'}$ and $\overline{u'w'}$ are direct measurements but $\overline{v'w'}$ is indirect

To acquire the near-wall velocity and stresses, we developed a high-spatial-resolution two-component laser-Doppler anemometer. The LDA optics, described in detail in Compton & Eaton (1996), produce a measuring volume that is 35 μm in diameter and approximately 66 μm long. This size was chosen to be comparable to the viscous length scale ν/u_τ for this flow, about 30 μm. The high resolution is achieved by placing the transmitting and receiving optics immediately below the test plate and reflecting the transmitted beams from a 1 cm $\times$ 1 cm mirror which is suspended in the flow downstream of the measurement location. This allows the use of short focal

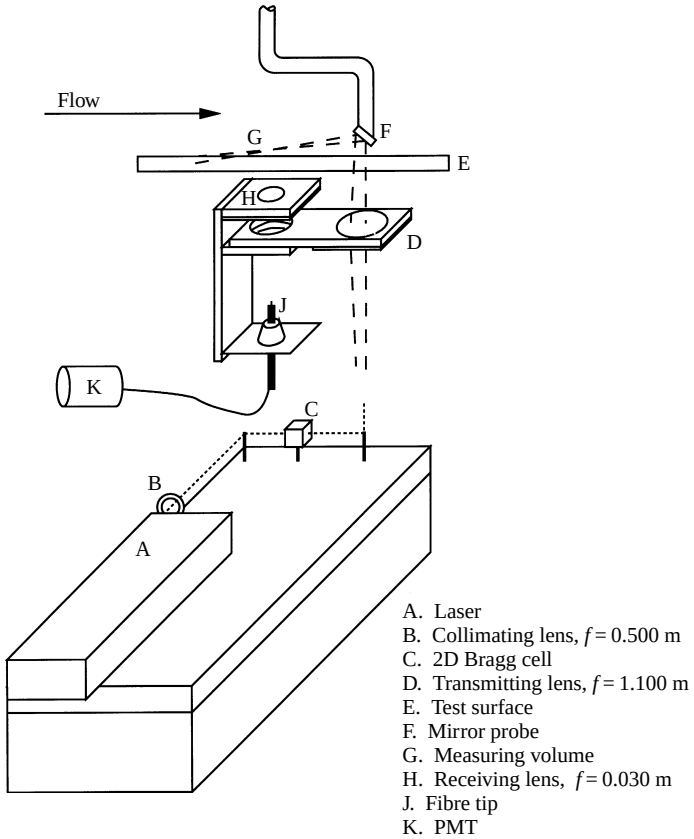

FIGURE 3. LDA optical path (not to scale).

length lenses and side-scatter collection, both of which serve to minimize the size of the measuring volume.

Figure 3 shows a sketch of the optical path for the LDA. The Bragg cell splits the collimated, single-frequency laser beam into three useful beams: a primary beam and two secondary beams. The frequencies of the two secondary beams are shifted by different amounts (typically 40 MHz and 41 MHz). The beams are focused by the transmitting lens, forming one set of fringes by crossing the primary beam with one of the secondary beams, and forming an orthogonal set of fringes by crossing the primary beam with the third beam. The optical arrangement ensures that the two sets of fringes are coincident. Light is collected in side scatter and focused onto the tip of an optical fibre which acts as the field stop and transmits the light to a photomultiplier tube. A Macrodyne 3102 frequency domain processor determines both velocity components by splitting the frequency range as suggested by Johnson (1990). Therefore, coincidence of the two-component velocity measurements is guaranteed. The two measured frequencies are passed to an IBM-compatible computer via GPIB. There are two configurations for the LDA optics: one produces simultaneous measurements of the U and V velocity components and the other measures the V and W components. With these two configurations, we directly measured the mean velocity, the Reynolds normal stresses, the $\overline{u'v'}$ and $\overline{v'w'}$ shear stresses, and triple products.

Quantity	Uncertainty
U, V ,W	$\pm$3% of U
$\overline{u'^2}$, $\overline{v'^2}$, $\overline{w'^2}$	$\pm$5% of $\overline{u'^2}$
$\overline{u'v'}$, $\overline{u'w'}$	$\pm$10% of $\overline{u'v'}$
$\overline{v'w'}$	$\pm$15% of $\overline{u'v'}$

TABLE 1. Crosswire uncertainties, from Anderson & Eaton (1989)

2.1. *Uncertainty*

Uncertainties in the near-wall LDA measurements arise from finite sample size, velocity bias, and finite spatial extent of the measuring volume. The statistical uncertainty in the mean at 95% confidence amounts to less than 1% of the mean velocity even in the region of highest relative turbulence intensity. The statistical uncertainty in the Reynolds stresses is approximately 4% of the measured stress. Adams, Eaton & Johnston (1984) developed a 'worst case' analysis of velocity bias, which yields for our system a peak error in the measured U of $0.8u_\tau$ at $y^+ = 7$. Their analysis is excessively conservative and the true bias is likely to be much smaller. Analysis (Compton & Eaton 1995) shows that the finite extent of the measuring volume is responsible for peak errors of approximately $0.1{u_\tau}^2$ in the normal stresses, and of $0.003u_\tau$ in the mean velocity, near the wall where the gradients are largest. The largest potential error in the Reynolds stress transport terms is due to inaccuracies in $\partial U/\partial y$ near the wall where the production terms are largest. At $y^+ = 10$ the potential error in $\partial U/\partial y$ is 3% of the calculated $\partial U/\partial y$, based on the calculated uncertainty in U.

In addition to the uncertainty mentioned above, there is a small systematic bias due to contributions to the stress measurements from $\overline{u'w'}$. The measuring volume was inclined 6° to the wall, which generated a crosstalk of $\overline{u'w'}$ with the other Reynolds stresses. The normal stresses $\overline{u'^2}$ and $\overline{w'^2}$ are off systematically by 3% of $\overline{u'w'}$, and the $\overline{u'v'}$ and $\overline{v'w'}$ shear stresses are off by approximately 12% of $\overline{u'w'}$. The $\overline{v'^2}$ and q^2 measurements are not affected by $\overline{u'w'}$. Of course, for two-dimensional boundary layers $\overline{u'w'}$ is identically zero. In the outer part of the boundary layer, we have crosswire measurements of $\overline{u'w'}$, which illustrate that the $\overline{u'w'}$ bias is small. Near the wall in a strongly turned boundary layer, $\overline{u'w'}$ can become as large as $\overline{u'v'}$, so $\overline{u'v'}$ and $\overline{v'w'}$ could be under-reported by as much as 12% of $\overline{u'v'}$. This would correspond to a maximum 15% error in $\overline{v'w'}$ for our farthest downstream station.

For three-hole probe measurements, Anderson & Eaton (1989) reported uncertainties in the measurements for a probe of identical design to be $\pm$0.2 m s^{-1} in velocity magnitude and $\pm$1.0° in direction. For crosswire measurements, we used the same probe tip as Anderson & Eaton (1989), and cite in table 1 the uncertainty levels which they assigned. Because $\overline{v'w'}$ is measured indirectly, that stress has the highest uncertainty.

3. Mean flow

Data are presented here for seven profile stations measured along the wind tunnel centreline. The most upstream station (A), located 17 in. upstream of the tip of the wedge, is taken as the reference position. The other measurement positions are listed in table 2. The x'-coordinate is the tunnel centreline with its origin at the reference location. The y-coordinate is normal to the wall, and the positive z-direction is

	Profile						
	A	C	D	E	F	G	H
x' (in.)	0	7.0	10.5	14.0	17.5	21.0	26.5
z (in.)	0	0	0	0	0	0	0
β (deg.)	0.14	1.81	3.52	5.63	7.90	10.57	14.36
Q_e (m s^{-1})	12.43	12.40	12.40	12.37	12.35	12.47	13.08
δ_{99} (mm)	36.3	38.5	41.6	43.1	45.2	49.5	56.5
δ^* (mm)	5.78	6.24	6.74	7.13	7.60	8.51	9.52
θ (mm)	4.22	4.56	4.90	5.19	5.53	6.19	7.04
$H \equiv \delta^*/\theta$	1.37	1.37	1.38	1.38	1.38	1.37	1.35
Re_{δ^*}	4692	5058	5458	5766	6136	6931	8139
Re_θ	3431	3693	3968	4192	4460	5047	6016
Q_τ (m s^{-1})	0.506	0.499	0.491	0.489	0.488	0.500	0.558
$C_f/2 \times 10^{-3}$	1.66	1.62	1.57	1.57	1.56	1.61	1.82
$C_f/2 \times 10^{-3}$ 2D†	1.63	1.60	1.57	1.55	1.53	1.48	1.42

† Formula for two-dimensional boundary layers based on Re_θ

TABLE 2. Boundary layer parameters from pressure data

chosen to form a right-handed coordinate system and points away from the wedge. The free-stream velocity at the reference position was 12.5 m s^{-1}.

The static pressure distribution is represented in terms of the pressure coefficient in figure 4(*a*):

$$C_p = \frac{p - p_{ref}}{\frac{1}{2}\rho {U_{ref}}^2}, \tag{3.1}$$

where p_{ref} and U_{ref} are the static pressure and free-stream velocity at the reference position. The data are plotted along lines of constant z with the centreline highlighted. The pressure rises approaching the wedge for negative values of z, but is nearly constant along the centreline until approximately $x' = 17$ and then falls off as the flow accelerates past the wedge. There is a strong spanwise pressure gradient upstream of the wedge, which acts to turn the flow into the angled exit passage. Figure 4(*b*) presents the derivatives of the static pressure in tunnel coordinates and in coordinates aligned with the local free-stream velocity.† For most of the boundary layer, $|\partial C_p/\partial z|$ is much greater than $|\partial C_p/\partial x|$. The streamwise pressure gradient is nearly zero up to measurement station E and remains small up to station F. The pressure gradient is strongly favourable beyond the wedge tip. The derivatives show the same basic behaviour in free-stream coordinates. The streamwise pressure gradient, $\partial C_p/\partial s$, is small compared to $\partial C_p/\partial n$, except toward the exit where the pressure gradient is predominantly streamwise. The strongest curvature is at station F, where $\delta_{99}\partial C_p/\partial n = -0.034$ and $\delta_{99}\partial C_p/\partial s = -0.010$. This is stronger turning than in the experiment of Schwarz & Bradshaw (1992), but weaker than that in Anderson & Eaton (1989).

The mean velocity magnitude profiles are featured in figures 5 and 6. In figure 5 the data are non-dimensionalized by Q_e and δ_{99}, both of which are listed in table 2. The velocity magnitude profiles look like ordinary boundary layer profiles until the last station (H) where there is clear evidence of an inner layer resulting from the

† We have defined (s, y, n) coordinates to be right-handed, a rotated version of the (x, y, z) tunnel coordinates. This makes n point inward toward the centre of curvature, which is not consistent with the usual casting of Euler's equation in streamline coordinates.

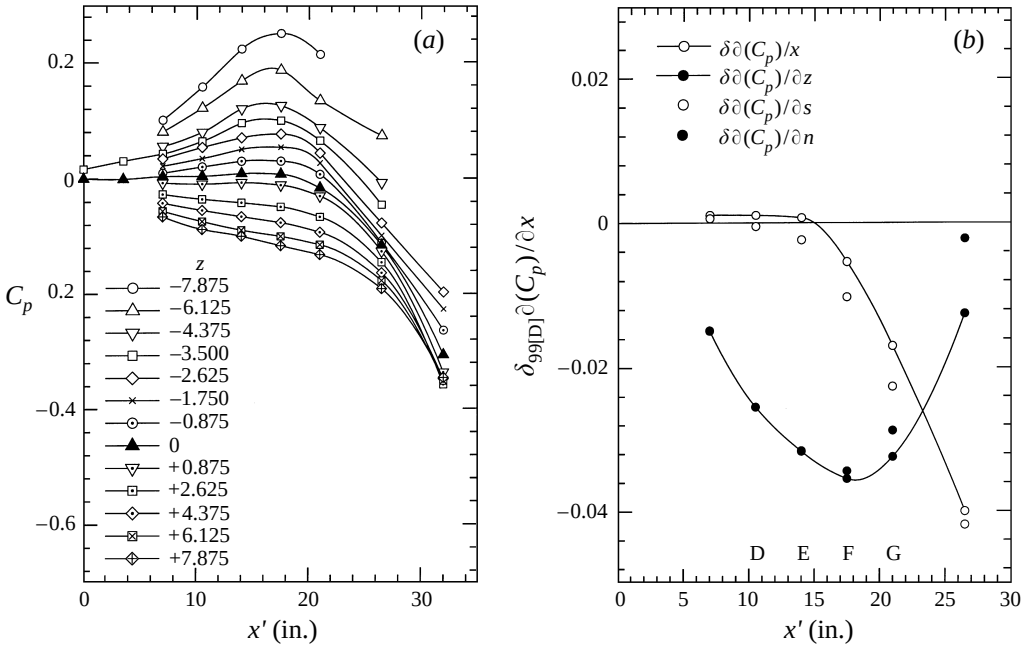

FIGURE 4. (*a*) Static pressure distribution near the wedge. (*b*) Static pressure derivatives, normalized by δ_{99} at station D. Wedge tip is at $x' = 17$ in.

imposition of a favourable pressure gradient. There has been considerable debate as to whether it is appropriate to expect three-dimensional boundary layers to conform to the law of the wall. Figure 6 is a relatively unbiased representation of the fit to the law of the wall. To calculate the friction velocity Q_τ we used the pressure data, and assumed that the law of the wall holds for the velocity magnitude:

$$Q/Q_\tau = \frac{1}{\kappa}\ln(yQ_\tau/\nu) + B. \tag{3.2}$$

Here, we used $\kappa = 0.41$ and $B = 5.0$. Our analysis program iterated to obtain constant Q_τ in the region $40 \leqslant y^+ \leqslant 150$. In reducing the LDA data, we determined the wall offset by optimizing the data's fit to $u^+ = y^+$, so the profile collapse in this region is not surprising. All the pressure profiles tend to rise above the line slightly at first, then dip below it. They then rise well above the line to form a 'wake' region. The profile at station G is mildly distorted by the favourable pressure gradient. Table 2 lists the skin friction coefficient determined from the profile fit, compared to the analytically predicted value for two-dimensional boundary layers, $C_f/2 = 0.0125Re_\theta^{-0.25}$ (Kays & Crawford 1980). The good agreement between the measured and predicted C_f at small turning angles indicates that we may expect some two-dimensional correlations to work in this region of three-dimensionality. The points farther downstream have skin friction coefficients greater than the two-dimensional correlation, indicating the favourable streamwise pressure gradient's influence on the mean velocity profiles.

Table 2 also lists the boundary layer integral parameters,

$$\delta^* \equiv \int_0^\infty \left(1 - \frac{U_s}{U_e}\right) \mathrm{d}y; \quad \theta \equiv \int_0^\infty \frac{U_s}{U_e}\left(1 - \frac{U_s}{U_e}\right) \mathrm{d}y. \tag{3.3}$$

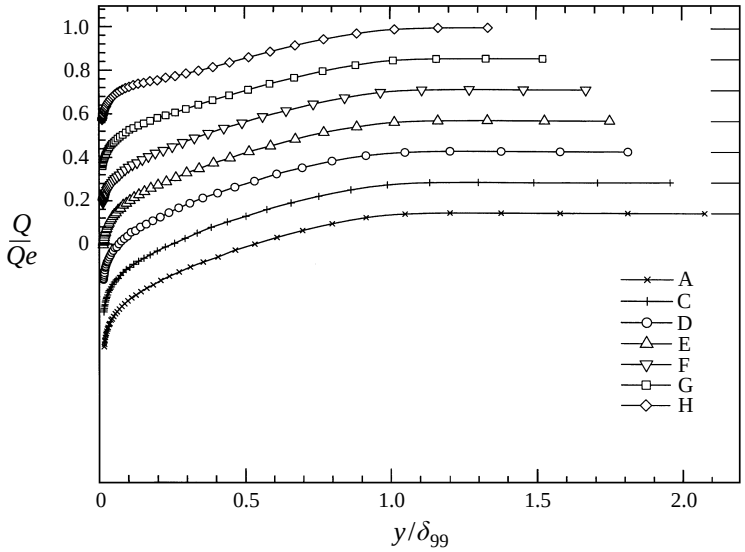

FIGURE 5. Velocity magnitude. Pressure data. Staggered axis; ticks on right axis indicate $Q/Q_e = 1$.

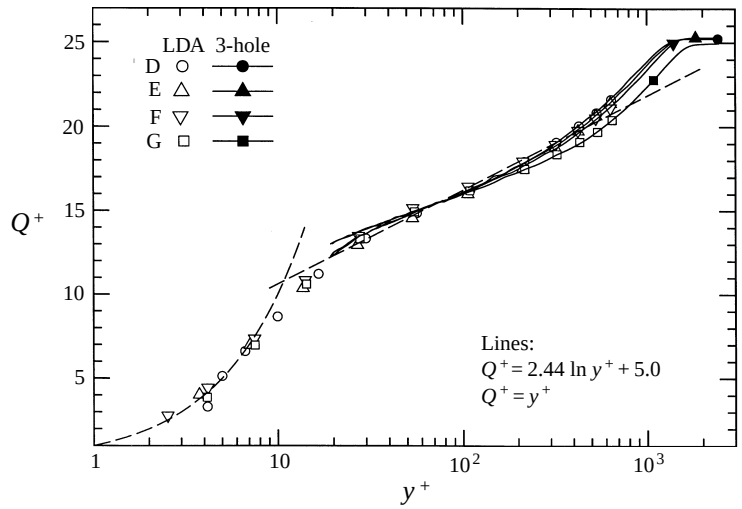

FIGURE 6. Law-of-the-wall representation. LDA data and pressure data.

The mean flow angle profiles are presented in figure 7, relative to the free-stream turning angle β (also tabulated in table 2). The turning angle $\gamma - \beta$ is positive, indicating that the flow near the wall is rotated at a greater angle than the free stream, as is expected. For the most part, $\gamma - \beta$ increases monotonically toward the wall down to about $y^+ = 20$, below which the angle is approximately constant, indicating the presence of a near-wall collateral region. At station G the trend of the angle reverses below $y^+ = 20$ with the angle decreasing toward the wall. At the farthest downstream station (H), the skewing through the boundary layer reaches a maximum of 24°. The turning angle decreases approaching the wall for much of the boundary layer at this station; this is related to the rapid reduction in the cross-stream pressure gradient. The LDA data show considerable scatter in the one or two

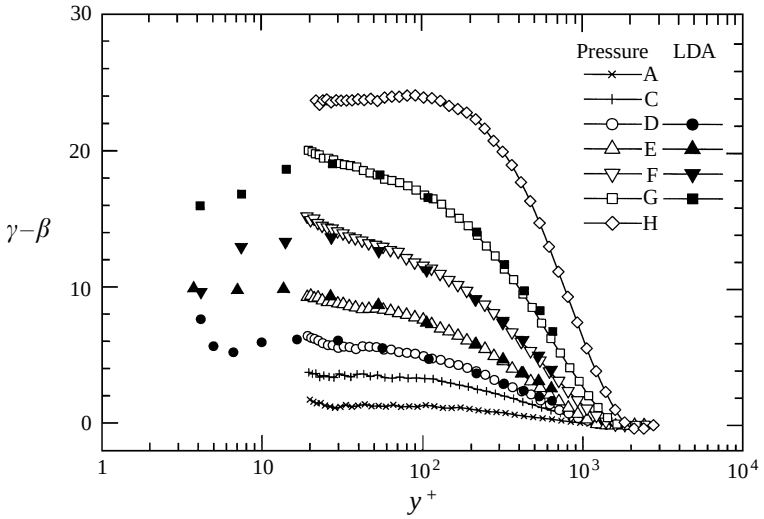

FIGURE 7. Mean velocity angle. LDA data and pressure data.

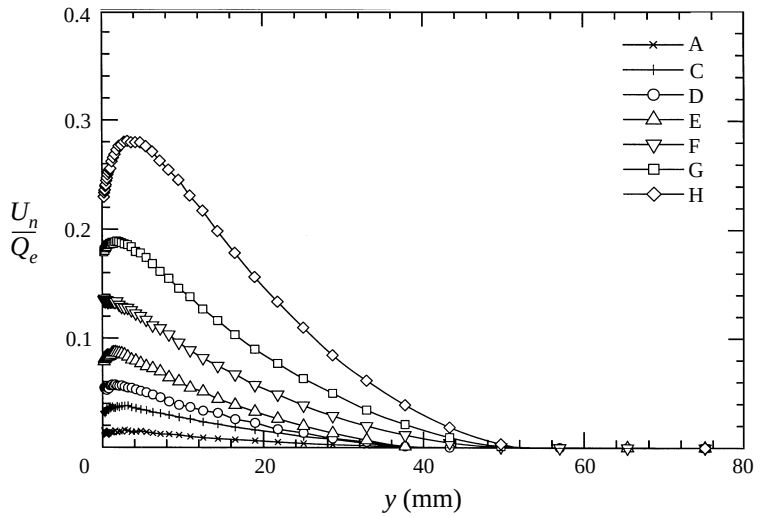

FIGURE 8. Spanwise velocity. Pressure data.

points nearest the wall. This is because different LDA setups are used to measure the U and W velocity components. A slight offset in the vertical positioning can result in significant error in the angle because of the steep velocity gradients near the wall.

The cross-stream velocity component $U_n(= W\cos\beta - U\sin\beta)$ is shown in figure 8. The location of maximum cross-stream velocity continues to move outward as the flow develops, even though the skewing is continually increasing.

We also represent the mean velocities using a hodograph, figure 9, which shows the spanwise component of velocity as a function of the streamwise component. The curves show an approximately triangular shape, as predicted by Johnston (1960). There is excellent agreement between the LDA data and the three-hole probe data throughout most of the boundary layer. Near the inner edge of the

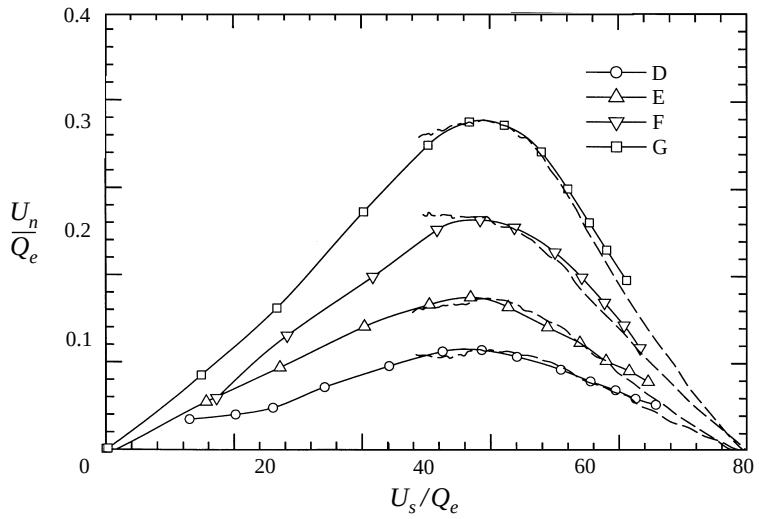

FIGURE 9. Hodograph. Dashed lines represent pressure data.

pressure profiles, agreement is not as good, most likely due to small angle errors in the three-hole probe data as the probe approaches the wall. The most striking feature of this plot is that the flow near the wall appears to be almost collateral.

4. Turbulence statistics

Turbulence quantities in the three-dimensional turbulent boundary layer were measured using both LDA and crosswires at stations D, E, F, and G. The Reynolds stresses are presented in the tunnel coordinate system, normalized by the friction velocity (as found using (3.2)) and plotted in semi-log coordinates against y^+ to emphasize near-wall features.

The Reynolds normal stresses are shown in figures 10(*a*)–10(*c*). The upstream profiles look much like two-dimensional boundary layer profiles, with $\overline{u'^2}$ consistently reaching a peak near $y^+ = 15$ (cf. Purtell & Klebanoff 1981; Spalart 1988), and with $\overline{w'^2}$ smaller than $\overline{u'^2}$, and $\overline{v'^2}$ smaller yet. The peak in $\overline{u'^2}$ diminishes in amplitude at the farthest downstream stations. There is general collapse among the $\overline{u'^2}$ data in the region below $y^+ = 10$. The $\overline{v'^2}$ data nearly collapse when scaled in wall coordinates: the three-dimensionality apparently does not have a strong effect on $\overline{v'^2}$. As the flow develops, the level of $\overline{w'^2}$ gradually increases, with a peak appearing in the near-wall region. At station G, this peak is near $y^+ = 15$. The agreement is generally quite good between the LDA data and the crosswire data in the region where the two datasets overlap.

Figure 11 shows the development of $q^2(\equiv \overline{u'^2} + \overline{v'^2} + \overline{w'^2})$ which reaches a peak near $y^+ = 10$, falls to a plateau in the range $40 < y^+ < 300$, then falls off steeply at the edge of the boundary layer. With increasing three-dimensionality, the plateau region appears to grow flatter, and in the outer part of the boundary layer we see a mild increase in turbulent kinetic energy. In the near-wall region the turbulent kinetic energy profiles collapse, indicating a trade-off between $\overline{u'^2}$ and $\overline{w'^2}$. This trade-off suggests simple rotation of the stress tensor, but our attempts to explain it in terms of rotation fail.

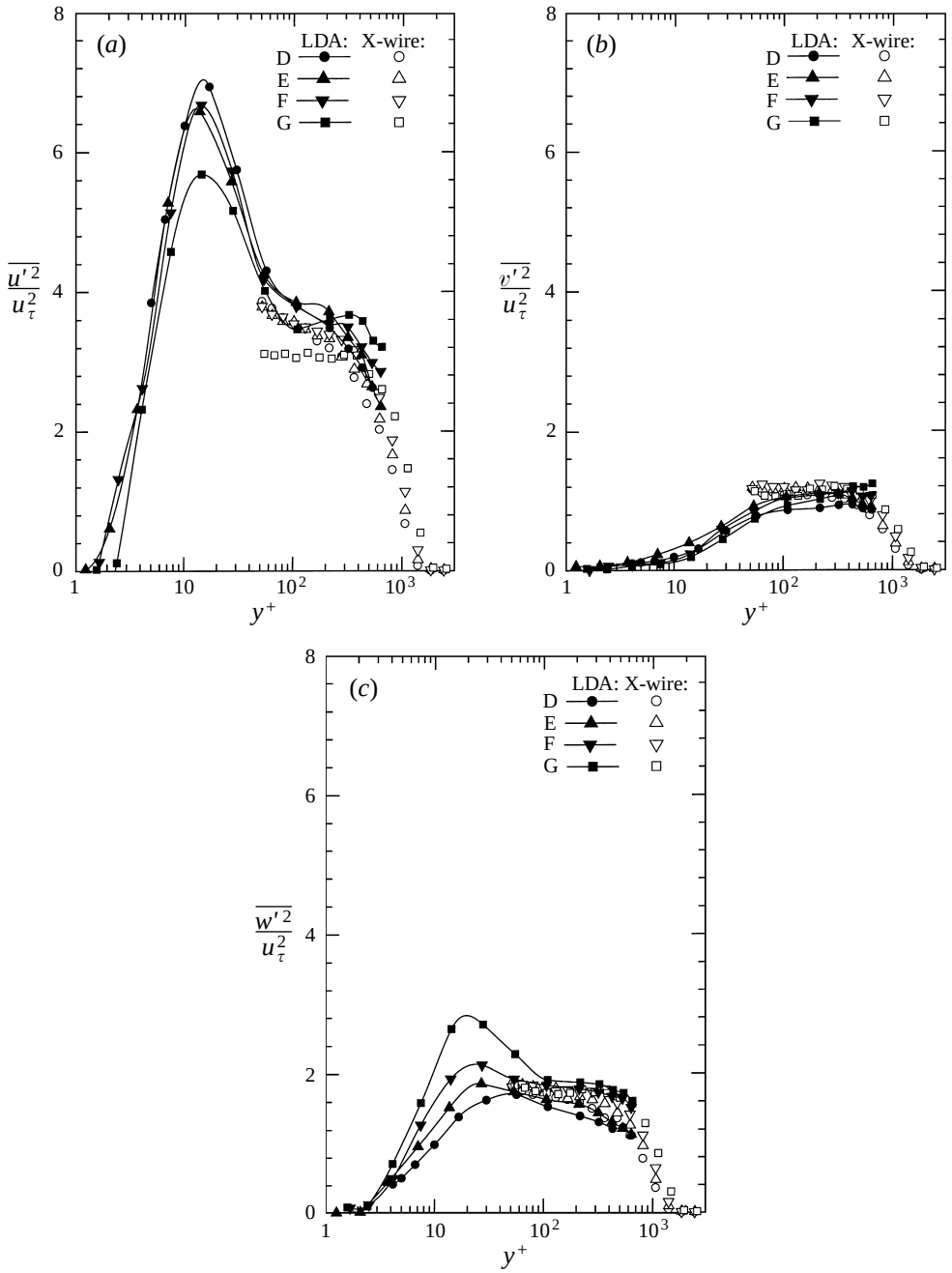

FIGURE 10. Reynolds normal stresses: (*a*) $\overline{u'^2}$, (*b*) $\overline{v'^2}$, (*c*) $\overline{w'^2}$.

Figures 12(*a*) and 12(*b*) show the streamwise and spanwise shear stresses. The $-\overline{u'v'}$ stress does not collapse as well in the region $y^+ < 10$ as the normal stresses do. Collapse of $-\overline{u'v'}$ in the near-wall region is not necessarily expected, since the streamwise pressure gradient will affect the shear stress. We note that there is a distinct decrease in $-\overline{u'v'}$ with increasing three-dimensionality. Our data differ from those of Flack & Johnston (1993), who observed shear stresses collapsing up to $y^+ = 50$. The

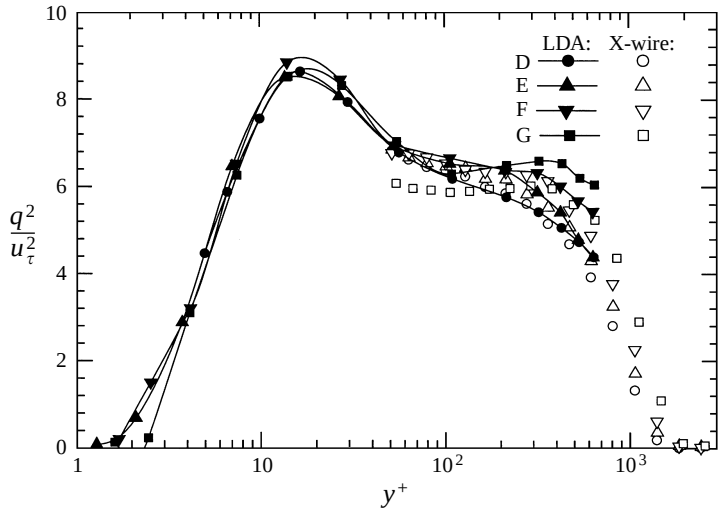

FIGURE 11. Turbulent kinetic energy.

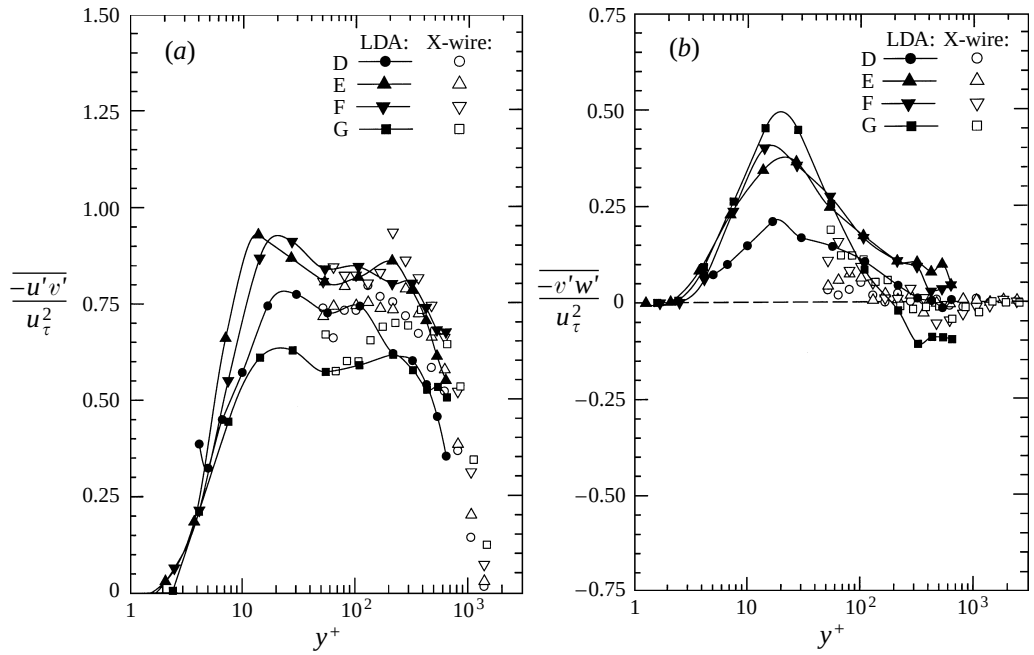

FIGURE 12. (*a*) $-\overline{u'v'}$ shear stress. (*b*) $-\overline{v'w'}$ shear stress.

$-\overline{v'w'}$ shear stress develops with increasing three-dimensionality. At station G the peak $-\overline{v'w'}/{u_\tau}^2$ is about 0.5 near $y^+ = 10$ to 20, which is almost as large as $-\overline{u'v'}/{u_\tau}^2$ at that point. We note that the crosswire fails to capture the major part of the $\overline{v'w'}$ stress.

4.1. *Angles of stress and strain*

An isotropic eddy viscosity formulation is only valid if the shear stress angle γ_τ ($\equiv \arctan(\overline{v'w'}/\overline{u'v'})$) is identical to the mean strain angle γ_g ($\equiv \arctan[(\partial W/\partial y)/(\partial U/\partial y)]$).

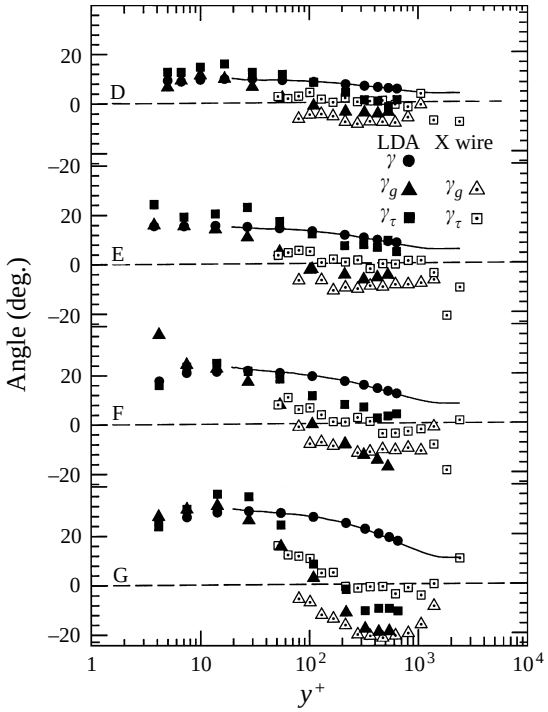

FIGURE 13. Flow angles at the four stations D, E, F and G. Solid lines indicate γ from pressure data.

These angles, along with the mean flow angle γ, are plotted in figure 13. Throughout most of the boundary layer, the angles of stress and strain do not agree. Most of the experiments in the literature demonstrated that the shear stress vector lagged the mean strain vector. Our data demonstrate the same lag through most of the boundary layer. Station F shows that $(\gamma_\tau - \gamma)$ is less than $(\gamma_g - \gamma)$ by as much as 20°. However, below $y^+ = 30$ the angles nearly coincide, and the difference between γ_τ and γ_g near $y^+ = 10$ is negligible. Below $y^+ = 8$ scatter prevents us from drawing further conclusions; some of the points nearest the wall have been omitted. Agreement between the flow angle γ and the gradient angle γ_g is not expected. However, if the flow is collateral at the wall, γ_g and γ should be the same in the viscous sublayer. The angle data uphold the idea of collateral flow at the wall, showing close agreement at all stations around $y^+ = 8$.

The eddy viscosity ratio N_e is used as a measure of the anisotropy of the turbulence, and can be used as the basis of a simple turbulence model. Usually, N_e is defined as the ratio of the spanwise eddy viscosity to the streamwise eddy viscosity in a coordinate system aligned with the local mean flow. It can be represented as

$$N_e \equiv \frac{\tan(\gamma_\tau - \gamma)}{\tan(\gamma_g - \gamma)}. \tag{4.1}$$

There are serious flaws with the concept: first, that two misaligned vector quantities should be related by a simple scalar proportion, and second, that a practicable coordinate system could everywhere have a different orientation throughout the flow field. We calculated N_e for these data and found that it is always

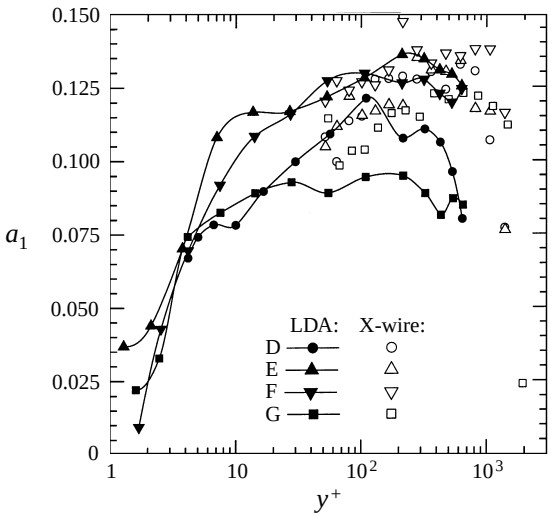

FIGURE 14. a_1 turbulence structure parameter.

less than 0.8 but varies broadly with no significant trend. Earlier experiments have shown the eddy viscosity ratio ranging between 0.1 and 1.2. The use of an anisotropic eddy viscosity model based on N_e is not supported by the present data.

4.2. *Structural parameters*

Figure 14 shows Townsend's structure parameter a_1, which can be thought of as the 'efficiency' of the turbulence in generating shear stress. The value of a_1 is generally around 0.15 for two-dimensional boundary layers, even in the presence of moderate pressure gradient, but many three-dimensional turbulent boundary layer studies have found a_1 to drop below that value. The crosswire data show the behaviour of a_1 in the outer part of the boundary layer. Near $y^+ = 1000$, a_1 is at its highest, ranging between 0.12 and 0.14. Profile G has the lowest values of a_1. The LDA data are noisier but also indicate suppressed values of a_1. It appears that reduced values of shear stress (figure 12*a*) are the cause of the suppression of a_1. Flack & Johnston observed that for their 30° bend flow, a_1 took on a consistent profile from the wall to about $y^+ = 50$, then fell to values around 0.11. We do not observe this near-wall agreement. This may be due to our experiment's higher Reynolds number and stronger curvature. The experimental uncertainty in the measurement of a_1 is quite high, so it is difficult to draw broader conclusions.

Figure 15(*a*) shows the turbulence structure parameter $(\overline{u'^2} + \overline{w'^2})/\overline{v'^2}$, which is also invariant to rotation about the y-axis. The value of this parameter is 2 in isotropic turbulence. In the present flow $(\overline{u'^2} + \overline{w'^2})/\overline{v'^2}$ is around 3 toward the outer edge of the boundary layer, and increases toward the wall. Owing to the wall's damping of $\overline{v'^2}$, eddies shift their turbulent kinetic energy from $\overline{v'^2}$ to the other two components. We find that the further downstream stations have significantly decreased values of $(\overline{u'^2} + \overline{w'^2})/\overline{v'^2}$. This trend suggests a marked tendency toward isotropy near the wall.

Figure 15(*b*) shows the ratio of wall-normal fluctuations to the shear stress magnitude, $\overline{v'^2}/\left(\overline{u'v'}^2 + \overline{v'w'}^2\right)^{1/2}$. Ölçmen & Simpson (1995) investigated this parameter

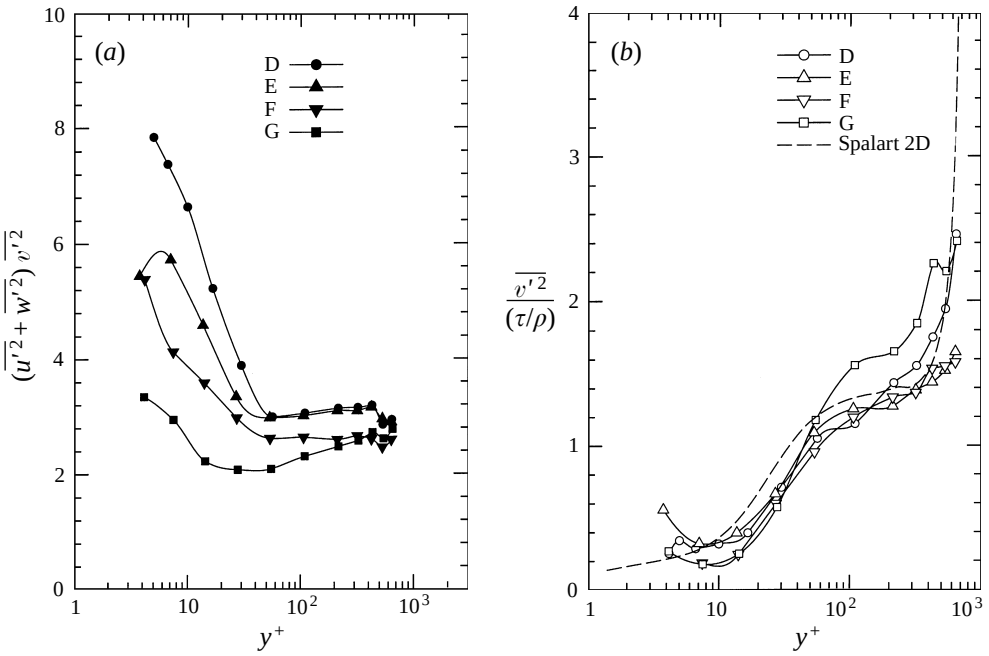

FIGURE 15. (*a*) $(\overline{u'^2}+\overline{w'^2})/\overline{v'^2}$ turbulence structure parameter; (*b*) $\overline{v'^2}/\tau$ turbulence structure parameter.

for their flow and for several others, and found a region of approximately constant $\overline{v'^2}/(\tau/\rho)$ above $y^+ = 50$ and below $y/\delta_{99} = 0.5$. Our data do not show this plateau region; instead they agree well with the two-dimensional boundary layer simulation of Spalart (1988). The present data, like Ölçmen & Simpson's, exhibit an upward trend for $y^+ < 8$, which must be a result of inaccuracies in the measurement system and not an artifact of three-dimensionality. Three-dimensionality apparently has little effect on $\overline{v'^2}/(\tau/\rho)$ for this flow.

5. Reynolds stress transport

The transport equation for turbulent kinetic energy is

$$U_k\frac{\partial(q^2)}{\partial x_k} = \overbrace{-2\overline{u_i'u_k'}\frac{\partial U_i}{\partial x_k}}^{\mathscr{P}_{ii}} + \overbrace{2\nu\overline{\frac{\partial u_i'}{\partial x_k}\frac{\partial u_i'}{\partial x_k}}}^{\mathscr{D}_{ii}} + \frac{\partial}{\partial x_k}\overbrace{\left[\frac{-2}{\rho}\overline{p'u_k'} - \overline{u_i'u_i'u_k'} - \nu\frac{\partial(q^2)}{\partial x_k}\right]}^{\mathscr{J}_{iik}}. \tag{5.1}$$

The advection, production, triple-product transport, and viscous transport terms were simplified and measured directly at stations D and G. Acquiring additional profiles allowed accurate calculation of streamwise and spanwise derivatives. These additional profiles form 'diamond' patterns, as indicated in figure 2. To calculate wall-normal derivatives, we used parabolic central first- and second-derivative formulas for unevenly spaced data.

To simplify the turbulent kinetic energy transport equation, production terms containing $\overline{u'w'}$ were eliminated following Pierce & Ezekewe (1976). Using the thin

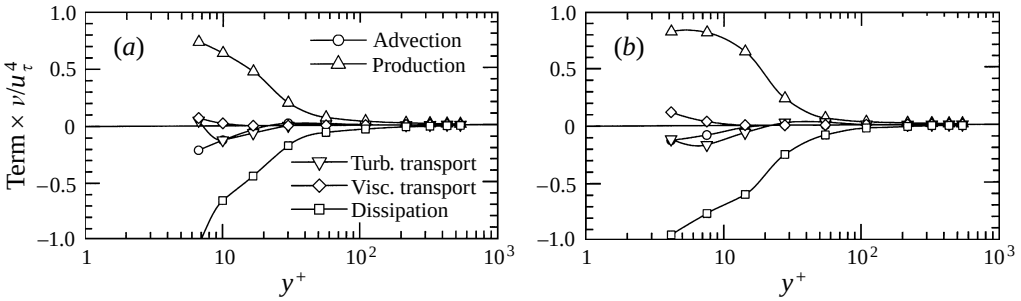

FIGURE 16. Terms of Reynolds stress transport equation for q^2, inner scaling: (*a*) station D, (*b*) station G.

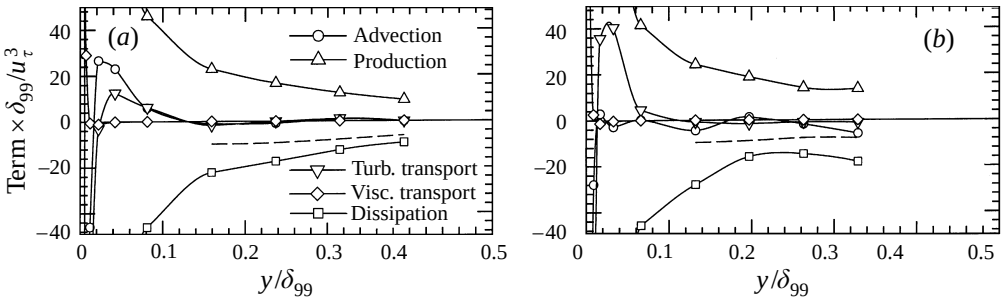

FIGURE 17. Terms of Reynolds stress transport equation for q^2, outer scaling. Dashed curve indicates two-dimensional dissipation rate correlation: (*a*) station D, (*b*) station G.

shear layer assumption to simplify the viscous transport term and order of magnitude arguments to simplify the production and triple product terms, the equation reduces to

$$\overbrace{\left(U\frac{\partial}{\partial x}+V\frac{\partial}{\partial y}+W\frac{\partial}{\partial z}\right)q^2}^{advection}=\overbrace{-2\left(\overline{u'v'}\frac{\partial U}{\partial y}\right)-2\left(\overline{v'w'}\frac{\partial W}{\partial y}\right)}^{production}+\overbrace{\mathscr{D}_{ii}}^{dissipation}$$
$$\overbrace{-\frac{\partial}{\partial y}(\overline{u'^2v'}+\overline{v'^3}+\overline{v'w'^2})}^{turbulent\ transport}\overbrace{-\nu\left(\frac{\partial^2 q^2}{\partial y^2}\right)}^{viscous\ transport} \tag{5.2}$$

where the dissipation term $\mathscr{D}_{ii}$ implicitly contains the pressure transport terms and is inferred by difference.

Figure 16(*a*, *b*) shows the transport terms for q^2 at stations D and G plotted in inner coordinates. Figure 17(*a*, *b*) shows the same data with a greatly expanded vertical scale to show the outer layer development. Experimenters usually present these terms in outer coordinates, without the near-wall measurements. It is obvious from figure 16 that the transport terms are orders of magnitude larger in the inner region than in the outer part of the log region and the wake.

The production and dissipation of turbulent kinetic energy are nearly balanced throughout the layer with a small contribution of viscous transport very near the wall. The peak production occurs very near the wall in both cases. The turbulent kinetic energy production should drop to zero at the wall, while the dissipation should not. There are small differences between the production rate profiles for the

two positions. Station G exhibits slightly higher production at $y^+ = 10$ and somewhat lower production at $y^+ = 100$ ($y/\delta \approx 0.08$). Moin *et al.* (1990) found suppression of turbulent kinetic energy production in their direct numerical simulation of a channel flow subjected to a suddenly applied transverse pressure gradient.

The advection, viscous transport, and turbulent (triple product) transport terms are generally much smaller than the production and dissipation terms. The advection and turbulent transport terms reach small (negative) peaks below $y^+ = 20$, with the advection reaching a peak closer to the wall than the turbulent transport. Spalart's (1988) two-dimensional boundary layer computation showed that advection should be negligible near the wall, while the turbulent transport reaches a negative peak around $y^+ = 10$. The viscous transport is important below $y^+ = 20$.

Also shown on figure 17 is an empirical relation for the dissipation which generally performs well in two-dimensional boundary layers:

$$\epsilon = \frac{(\tau/\rho)^{3/2}}{0.1\,\delta_{99}}. \tag{5.3}$$

Bradshaw & Pontikos (1985), Littell & Eaton (1994), and Schwarz & Bradshaw (1992) all showed that this relation underpredicts the actual dissipation rate in the region $y/\delta_{99} \leqslant 0.4$. The present data show the same trend with the underprediction worsening close to the wall.

The measurements of the transport terms for the two main shear stresses are presented in detail in Compton & Eaton (1995). The terms in the $\overline{u'v'}$ were found to agree reasonably well with the two-dimensional boundary layer simulation results of Spalart (1988) at station D. However, production was reduced by 10% to 20% near the wall at station G, balanced by changes in the pressure–strain term. We also derived a transport equation for a_1 and found that the production term is approximately

$$\mathscr{P}_{a_1} \approx \left(2\left(\frac{\tau}{\rho}\right)^2 - \overline{v'^2}q^2\right)\frac{1}{q^4\tau/\rho}\left(\overline{u'v'}\frac{\partial U}{\partial y} + \overline{v'w'}\frac{\partial W}{\partial y}\right). \tag{5.4}$$

Our data also indicate that this term is reduced near the wall in our flow. A model based on a_1 transport may thus be capable of accounting for the reduction of shear stresses observed in most three-dimensional turbulent boundary layers.

6. Summary

We have examined a three-dimensional turbulent boundary layer formed by turning an initially two-dimensional boundary layer by a strong spanwise pressure gradient. The streamwise pressure gradient was initially very mild but became strongly favourable by the final station studied. The near-wall measurements obtained using a special high-resolution LDA have revealed several features of the boundary layer that have not previously been observed. First, we have observed a nearly collateral region in the mean velocity profile below $y^+ = 20$. This results in an alignment of the flow angle and the velocity gradient angle in the viscous sublayer. More importantly, the shear stress vector aligns with the velocity gradient vector below $y^+ = 20$ suggesting that a scalar eddy viscosity is appropriate for the crucial near-wall region. Outside the near-wall region, the directions of the shear stress and strain rate vectors deviate by as much as 20°.

As the three-dimensionality develops, the $\overline{w'^2}$ profile grows a peak near $y^+ = 10$. The increase in $\overline{w'^2}$ nearly makes up for the decrease in $\overline{u'^2}$ so the turbulent kinetic energy is only mildly suppressed in the near-wall region. The shear stresses are more strongly affected by three-dimensionality. The streamwise shear stress $-\overline{u'v'}$ begins much like a two-dimensional boundary layer. With increasing three-dimensionality, it displays a marked decrease, by as much as 30%. The spanwise shear stress grows to peak values as high as $0.5u_\tau^2$. Both components of the shear stress vector show collapse very near the wall ($y^+ < 10$) in inner coordinates, but they diverge above that region. The structural parameter a_1 is suppressed throughout most of the boundary layer, since the magnitude of the shear stress decreases more than the magnitude of the turbulent kinetic energy.

Correct modelling of the near-wall region is crucial since that zone dominates the production of turbulence, contains the highest shear stress gradients, and accounts for most of the displacement thickness. The present study shows that the near-wall turbulence behaviour cannot be inferred by extrapolating trends from measurements in the logarithmic and wake regions. The present near-wall measurements have not been corroborated by other studies. Flack & Johnston (1993) found considerably different results in a boundary layer at much lower Reynolds number and with milder skewing. Further studies capable of resolving the near-wall region of three-dimensional turbulent boundary layers are needed in order to develop appropriate models capable of realistically capturing three-dimensional effects.

This work was supported by the Department of Energy (grant number DE-FG03-93ER14317-A000) and NASA-Ames Research Center (grant number NCC2-5001). We also extend our gratitude to Professor Peter Bradshaw for his input on Reynolds stress transport.

REFERENCES

Adams, E. W., Eaton, J. K. & Johnston, J. P. 1984 An examination of velocity bias in a highly turbulent separated and reattaching flow. In *Laser Anemometry in Fluid Mechanics*, pp. 21–37 Ladoan – Instituto Superior Técnico 1096 Lisboa Codex, Portugal.

Anderson, S. D. & Eaton, J. K. 1989 Reynolds stress development in pressure-driven three-dimensional turbulent boundary layers. *J. Fluid Mech.* **202**, 263–264.

Bettelini, M. S. G. & Fanneløp, T. K. 1993 Systematic comparison of mathematically simple turbulence models for three-dimensional boundary layers. *AIAA J.* **31**, 999–1006.

Bradshaw, P. & Pontikos, N. S. 1985 Measurements in the turbulent boundary layer on an 'infinite' swept wing. *J. Fluid Mech.* **159**, 105–130.

Compton, D. A. & Eaton, J. K. 1995 Near-wall measurements of a three-dimensional turbulent boundary layer. *Stanford Univ. Dept. Mech. Engng Thermosciences Div. Rep.* MD-72.

Compton, D. A. & Eaton, J. K. 1996 A high-resolution laser Doppler anemometer for three-dimensional turbulent boundary layers. *Exps. Fluids* **22**, 111–117.

Degani, A. T., Smith, F. T. & Walker, J. D. A. 1993 The structure of a three-dimensional turbulent boundary layer. *J. Fluid Mech.* **250**, 43–68.

Eaton, J. K. 1995 The effects of mean flow three dimensionality on turbulent boundary layer structure. *AIAA J.* **33**, 2020–2025.

Flack, K. A. & Johnston, J. P. 1993 Near-wall investigation of three-dimensional turbulent boundary layers. *Stanford Univ. Dept. Mech. Engng Thermosciences Div. Rep.* MD-63.

Johnson, D. A. 1990 Simultaneous multivelocity component laser Doppler velocimetry using one digital frequency processor. *Rev. Sci. Instrum.* **61**, 1989–1990.

Johnston, J. P. 1960 On the three-dimensional turbulent boundary layer generated by secondary flow. *Trans. ASME J. Basic Engng* March 1960, 233–248.

Johnston, J. P. 1976 Experimental studies in three-dimensional turbulent boundary layers. *Stanford Univ. Dept. Mech. Engng Thermosciences Div. Rep.* MD-34.

Kays, W. M. & Crawford, M. E. 1980 *Convective Heat and Mass Transfer*, 2nd edn McGraw-Hill.

Littell, H. S. & Eaton, J. K. 1994 Turbulence characteristics of the boundary layer on a rotating disk. *J. Fluid Mech.* **266**, 175-207.

Moin, P., Shih, T.-H., Driver, D. & Mansour, N. N. 1990 Direct numerical simulation of a three-dimensional turbulent boundary layer. *Phys. Fluids* A **2**, 1846–1853.

Murlis, J., Tsai, H. M. & Bradshaw, P. 1982 The structure of turbulent boundary layers at low Reynolds numbers. *J. Fluid Mech.* **122**, 13–56.

Ölçmen, M. S. & Simpson, R. L. 1992 Perspective: On the near wall similarity of three-dimensional turbulent boundary layers. *Trans. ASME J. Fluids Engng* **114**, 487–495.

Ölçmen, M. S. & Simpson, R. L. 1993 Evaluation of algebraic eddy-viscosity models in three-dimensional turbulent boundary layer flows. *AIAA J.* **31**, 1545–1554.

Ölçmen, M. S. & Simpson, R. L. 1994 A 5-velocity-component laser-Doppler velocimeter for measurements of a three-dimensional turbulent boundary layer. *7th Intl Symp on Applications of Laser Techniques to Fluid Mechanics, Jul. 11–14, 1994, Lisbon, Portugal.*

Ölçmen, M. S. & Simpson, R. L. 1995 An experimental study of a three-dimensional pressure-driven turbulent boundary layer. *J. Fluid Mech.* **290**, 225–262.

Pierce, F. J. & Ezekewe, C. I. 1976 Measured $\overline{uw}$ stress gradients in a three-dimensional turbulent boundary layer. Trans. *ASME J. Fluids Engng* **98**, 768–770.

Purtell, L. P. & Klebanoff, P. S. 1981 Turbulent boundary layer at low Reynolds number. *Phys. Fluids* **24**, 802–811.

Rotta, J. C. 1977 A family of turbulence models for three-dimensional thin shear layers. *1st Turbulent Shear Flow Symposium, Apr. 18–20, 1977, University Park, Pennsylvania.*

Schwarz, W. R. & Bradshaw, P. 1992 Three-dimensional turbulent boundary layer in a 30 degree bend: experiment and modelling. *Stanford Univ. Dept. Mech. Engng Thermosciences Div. Rep.* MD-61.

Schwarz, W. R. & Bradshaw, P. 1994 Term-by-term tests of stress-transport turbulence models in a three-dimensional turbulent boundary layer. *Phys. Fluids* **6**, 986–998.

Sendstad, O. & Moin, P. 1992 The near-wall mechanics of three-dimensional turbulent boundary layers. *Stanford Univ. Dept. Mech. Engng Thermosciences Div. Rep.* TF-57.

Spalart, P. R. 1988 Direct simulation of a turbulent boundary layer up to $R_\theta = 1410$., *J. Fluid Mech.* **187**, 61–98.

Webster, D. R., DeGraaff, D. B. & Eaton, J. K. 1996 Turbulence characteristics of a boundary layer over a swept bump. *J. Fluid Mech.* **323**, 1–22.

Westphal, R. V. & Mehta, R. D. 1985 Crossed hot-wire data acquisition and reduction system. *NASA TM* 85871.